Geochimica et Cosmochimica Acta 375 (2024) 173–185

Contents lists available at ScienceDirect

Geochimica et Cosmochimica Acta

journal homepage: www.elsevier.com/locate/gca

Phosphate uptake is an essential process for rapid bone mineralization during early diagenesis – evidence from bone alteration experiments

Anna G. Kral [a,*], Thorsten Geisler [a], Michael Wiedenbeck [b], Paul Guagliardo [c], Thomas Tütken [d]

[a] Institut für Geowissenschaften, Rheinische Friedrich-Wilhelms-Universität, Poppelsdorfer Schloss, Meckenheimer Allee 169, 53115 Bonn, Germany
[b] Helmholtz Zentrum Potsdam, Deutsches GeoForschungZentrum, GFZ, Telegrafenberg, 14473 Potsdam, Germany
[c] Centre for Microscopy, Characterization, and Analysis, The University of Western Australia, 35 Stirling Highway, Perth, WA 6009, Australia
[d] Institut für Geowissenschaften, Johannes-Gutenberg-Universität, Johann-Joachim-Becher-Weg 21, 55128 Mainz, Germany

ARTICLE INFO

Associate editor: Ruth E. Blake

Keywords:
Bone fossilization
Oxygen isotope composition
Raman spectroscopy
Secondary ion mass spectrometry
Isotope ratio infrared spectroscopy

ABSTRACT

Bones and teeth are often the only fossil remains of vertebrates that are preserved over geological time in sedimentary rocks. They render valuable archives for geochemical proxies which are commonly used for paleoreconstructions. However, the fossilization mechanisms of bone are not yet well understood. Crucial processes are the transformation of bioapatite into and the replacement of collagen by thermodynamically more stable apatite phases, such as fluorapatite. In the present study, aqueous alteration experiments on cortical bone samples were performed under simulated early diagenetic conditions in order to investigate whether and how an external phosphate (PO_4) source affects *post mortem* bone mineralization. Additionally, abiotic oxygen isotope exchange mechanisms between bioapatite and aqueous solutions were assessed by using either ^{18}O-enriched water or PO_4 as a tracer. The presence of an external sedimentary ^{18}O-labeled PO_4 source led to a rapid formation of new fluorapatite crystallites at the sample's margin that was highly enriched in ^{18}O. Meanwhile, in the interior of the samples carbonate-poor hydroxylapatite formed through a dissolution-precipitation process without incorporating significant amounts of the ^{18}O tracer. These two processes appear to act independently from each other. In samples exposed to ^{18}O-labeled aqueous solutions lacking a PO_4 source, no newly grown apatite crystallites were found, however in the interior of these samples, nano-crystalline carbonate-poor or -free hydroxylapatite precipitated. A comparatively low but uniform ^{18}O-enrichment was measured from the sample's margin towards its interior, which is assumed to have resulted from the adsorption of $H_2^{18}O$ onto crystallite surface sites and collagen. Overall, our results suggest that a fast incorporation of ^{18}O-doped PO_4 from the sediment source accelerated bone mineralization and consequently changed the oxygen isotope composition of the PO_4 group in the bone mineral phase more rapidly and to a greater extent than in a diagenetic setting lacking additional external PO_4. Dissolved PO_4 from the taphonomic setting thus seems to be an important factor fostering bone fossilization and preservation as well as oxygen isotope alteration.

1. Introduction

During fossilization the skeletal tissues of vertebrates are altered by various physicochemical processes, sometimes transforming the material in a way that allows bones to survive for millions of years in the fossil record. Such fossil remains represent valuable archives for paleoenvironmental or paleobiological information. For instance, the oxygen isotope composition ($\delta^{18}O$) of the phosphate (PO_4) and carbonate (CO_3) groups in bioapatite is used to infer past climate conditions (e.g., Longinelli, 1984; Kohn, 1996; Gehler et al., 2012; Lécuyer et al., 2013; Wierzbowski, 2021), the (thermo)physiology of vertebrates (e.g., Barrick and Showers, 1994; Stoskopf et al., 2001; Amiot et al., 2006; Bernard et al., 2010; Pack et al., 2013; Seon et al., 2022; Feng et al., 2022) or to assess the diagenetic alteration of bioapatite (Iacumin et al., 1996, 2022; Tütken et al., 2008; Pellegrini et al., 2011; PO_4 triple oxygen isotope composition: Gehler et al., 2011).

Living bone tissue consists predominantly of a carbonated calcium-phosphate mineral (55–60 wt%), approximated as hydroxylapatite (HAp) and commonly referred to as bioapatite, with a composition similar to dahllite ($Ca_{10}(CO_3, PO_4)_6(OH)_2$) (Wopenka and Pasteris,

* Corresponding author.
E-mail addresses: akral@uni-bonn.de (A.G. Kral), tgeisler@uni-bonn.de (T. Geisler), michael.wiedenbeck@gfz-potsdam.de (M. Wiedenbeck), paul.guagliardo@uwa.edu.au (P. Guagliardo), tuetken@uni-mainz.de (T. Tütken).

https://doi.org/10.1016/j.gca.2024.04.004
Received 6 March 2023; Accepted 3 April 2024
Available online 6 April 2024

2005). These crystallites are aligned within an organic scaffolding of primary type-I collagen fibers (≈ 30 wt%) (Tzaphlidou, 2008). Furthermore, living bone also contains 10–15 wt% of water (Rogers and Zioupos, 1999). Immediately *post mortem* bone taphonomy starts, either leading to the bone's preservation or, more likely, to its decomposition (Keenan, 2016; Dauphin, 2022). The fossilization process during which bone is preserved can be divided into two main stages: early and late diagenesis, which are differentiated by changes in the chemical environment and bone composition (Pfretzschner, 2004). Early diagenesis is characterized by abiotic and biotic decay of soft tissues, loss of bone collagen, and the modification of bioapatite (Collins et al., 2002; Trueman and Martill, 2002; Trueman and Tuross, 2002; Pfretzschner, 2006; Jans, 2008; White et al., 2014; Turner-Walker, 2019; Procopio et al., 2021). Once the organic matrix has been almost entirely replaced by minerals, late diagenesis sets in, characterized by the infilling of bone cavities, such as pore space or cracks, by secondary minerals (Pfretzschner, 2001a, b; Pfretzschner and Tütken, 2011). Whether or not a given bone is preserved or decomposes largely depends on the environmental conditions during early diagenesis (Nielsen-Marsh and Hedges, 2000; Berna et al., 2004; Trueman et al., 2004; Kohn, 2008).

Essential for the preservation of bone is the transformation of bioapatite into and the replacement of collagen by thermodynamically stable apatite such as fluorapatite (FAp), carbonated fluorapatite (CO_3-FAp), or similar stable apatite phases (Elorza et al., 1999; Berna et al., 2004; Nemliher et al., 2004; Goodwin et al., 2007; Pasteris and Ding, 2009). However, collagen, which constitutes *ca.* 30 wt% but up to 50 vol % of bone *in vivo*, is degraded during early diagenesis by chemical and biological processes (Collins et al., 2002; Hedges, 2002; Pfretzschner, 2006; Trueman et al., 2008), creating large volumes of additional pore space that must be filled by secondary apatite if preservation is to take place. This implies that vast amounts of exogenous Ca and PO_4 are required in order to lead to preservation. However, it remains unknown if the Ca and PO_4 for bone fossilization is derived from a redistribution within or among bones or from an external source such as diagenetic waters or the surrounding soil and sediment. The latter could distinctly alter the oxygen isotope composition, the former probably not. Already two decades ago, bone mineralization with new HAp or FAp by Ca and PO_4 derived from a mineral source of the burial environment was proposed to be an essential step for bone fossilization (Trueman and Tuross, 2002). However, systematic experiments investigating bone mineralization under early diagenetic conditions to test this hypothesis have not so far been conducted. In view of growing use of oxygen isotope ratios as paleoenvironmental archives, it seems essential that it is established whether bioapatite oxygen isotope composition can be shifted by recrystallization processes or by a widespread mineralization with exogenous PO_4.

Here, it should be mentioned that the term recrystallization, in its proper sense, refers to a solid-state process by which the physical structure of a crystal is changed under high pressures or temperatures without any dissolution step, meaning that the composition remains unchanged (Spry, 1969). However, in the context of fossilization, recrystallization is widely used as a generic term for modifications of the bone's mineral phase in an aqueous milieu. In the following paragraph, the main processes which can alter the mineral phase in bone are therefore briefly reviewed and the terminology is defined.

In the presence of an aqueous solution, bioapatite can be modified or replaced by interface-coupled dissolution-precipitation, i.e., the dissolution of a parent (here: bioapatite) is temporally and spatially coupled to the (re-)precipitation of a product phase (here: authigenic apatite) at an inwardly migrating dissolution-precipitation front (Putnis, 2002, 2009; Putnis and Putnis, 2007, 2022; Ruiz-Agudo et al., 2014). It is important to mention that such an interface-coupled dissolution-precipitation process may lead to the pseudomorphic replacement of nanometer-sized bioapatite crystallites (Kolodny et al., 1996; Putnis, 2002, 2009; Putnis and Putnis, 2007, 2022). Spatially decoupled dissolution-precipitation is also a possible mechanism when nucleation or crystal growth are locally inhibited, resulting in the dissolved material being transported away from the dissolving apatite to subsequently be reprecipitated far from its origin (Xia et al., 2009; Putnis, 2021). In addition, the attachment of authigenic and allothigenic apatite to biogenic apatite crystallites (Hubert et al., 1996; Trueman et al., 2004) can also alter the mineralogical composition of bone. Here, unless necessary for reasons of clarity, only recrystallization and mineralization will be distinguished for the sake of simplicity. We use the term recrystallization for all processes that primarily cause a transformation of bioapatite into another authigenic apatite phase without incorporating large amounts of external components. Mineralization is the formation of new allothigenic minerals from predominantly external components (e.g., PO_4 or F).

In the present study, the origin of PO_4 for bone mineralization was assessed by isothermal, heat-accelerated (60 and 90 °C) *in vitro* aqueous alteration experiments on modern ostrich cortical bone (CB). In our first series of experiments, bone was altered in a solution that also contained artificial sediment with ^{18}O-doped calcium hydrogen phosphate (CHP). Here, ^{18}O was used as a tracer to relate apatite growth to different sources of PO_4, i.e., external ^{18}O-doped PO_4 from the CHP in the sediment and internal PO_4 mobilized by the dissolution of bioapatite. This approach can also be used to distinguish between recrystallization and mineralization of bone because the solution itself was not enriched in $H_2^{18}O$, and oxygen in aqueous PO_4 only slowly exchanges with water (O'Neil et al., 2003; Geisler et al., 2009) at a temperature below 90 °C and within only one month ($t_{1/2}$ = 380 d at 75 °C and 23 d at 100 °C, Lécuyer et al., 1999). The initial dissolution of sediment-borne CHP leads to a release of Ca and PO_4 ions (ratio 1:2) into the solution, (super-) saturating the solution with HAp components and finally leading to the precipitation of new apatite species (Martin and Brown, 2005). Consequently, newly grown ^{18}O-rich apatite can be directly linked to the transfer of ^{18}O-enriched PO_4 from the sediment via the solution. Such an addition of external PO_4 may constitute a significant process for bone fossilization in natural sedimentary environments, but this has not yet been documented experimentally. In the second series of experiments, instead of the artificial sediment with ^{18}O-enriched PO_4, only $H_2^{18}O$ was used. Thus, due to the absence of an external PO_4 source, the only mechanism that could lead to the transformation from bioapatite to a different, more stable apatite phase, is recrystallization - or rather the processes summarized under this term. Therefore, recrystallization of bioapatite in an ^{18}O-labeled but PO_4-free solution is not expected to result in significant enrichment of ^{18}O, although some abiotic oxygen isotope exchange may occur via the CO_3 group, which is less stable under diagenetic conditions (Zazzo et al., 2004). Hence, our experimental approach could distinguish whether the oxygen isotope composition in bone is modified if only $H_2^{18}O$ is available and no ^{18}O-doped PO_4. Furthermore, we investigated how the bone was mineralogically modified in the absence of any external PO_4 source.

Using these two experimental setups the present study investigates (1) whether bone can be mineralized with PO_4 from an external source, (2) how bone changes mineralogically when no external PO_4 source is present, and (3) the effects of both scenarios on the oxygen isotope composition of bone under early diagenetic conditions.

2. Materials and methods

The CB samples and experimental solutions investigated in this study were derived from alteration experiments conducted in a previous study (Kral et al., 2021).

2.1. Experimental setup

Cylindrical CB samples were drilled from the compacta of a tibia of a modern ostrich (Fig. 1) that were then immersed in freshwater-like (FW), seawater-like (SW), and freshwater-like with added sediment (FWS) solutions. These solutions were designed to cover the range of

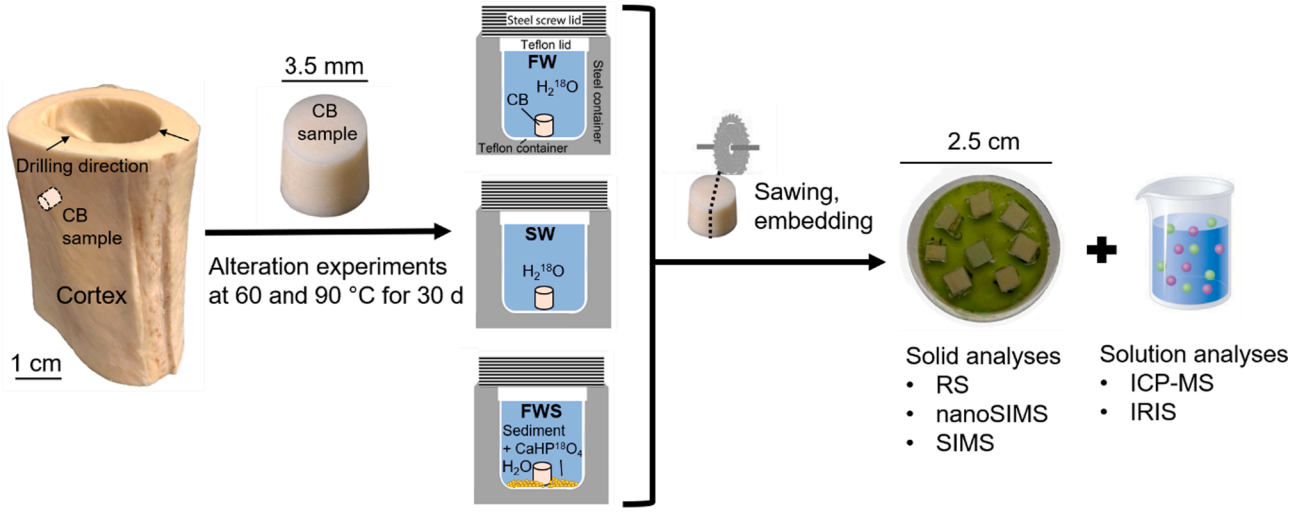

Fig. 1. Illustration of the experimental setup. Cylindrical cortical bone (CB) samples were drilled from the bone's cortex. The CB samples were placed in 3 mL Teflon© beakers containing 2 mL of ^{18}O-enriched freshwater (FW) and seawater (SW) solutions or 3 mL of the freshwater solution with sediment (FWS), which contained artificial sediment with ^{18}O-enriched PO_4. The beakers were placed in a steel container for up to 30 d at 60 and 90 °C. The CB samples were then cut into halves and embedded in mounts using Technovit© 5071 for further geochemical and isotopic analyses. RS = Raman spectroscopy, IRIS = isotope ratio infrared spectroscopy, (nano)SIMS = (nanoscale) secondary ion mass spectrometry, ICP-MS = inductively coupled plasma-mass spectrometry.

typical natural, near-surface water compositions. The original experiments ran for up to 30 d at 30, 60, and 90 °C to artificially accelerate the reaction and transport processes. In the present study, only CB samples from 60 and 90 °C experiments that ran for 30 d were considered because they exhibited the most significant structural and chemical changes (Kral et al., 2021, 2022). The experimental solutions contained several elements that are usually present in an early diagenetic setting and which can be incorporated into CB *post mortem*, such as F, Zn, Sr, rare earth elements, and U (e.g., Hedges, 2002; Trueman and Tuross, 2002; Herwartz et al., 2011; Simpson et al., 2021).

2.2. Experimental solutions

Both, FW and SW stock solutions (Table 1) were labeled with $H_2^{18}O$ containing 97 at.% ^{18}O (Rotem GmbH, Leipzig, Germany) at a ratio of 2 mL of 97 at.% $H_2^{18}O$ to 100 mL of purified water from a Millipore Milli-Q lab water system. This system meets the ASTM Type I water with 18.2 MΩ electric resistance, reflecting high ionic purity, and <50 ppb of Total Organic Carbons (TOC). The solutions had initial $\delta^{18}O$ values of 5,238 ± 21 ‰ and 5,491 ± 28 ‰, respectively. For the second series of experiments, a solution with a chemical composition similar to the FW solution (Table 1) was prepared that contained artificial sediment as an additive, i.e., FWS (Kral et al., 2021). In this case the solution itself was not labeled with $H_2^{18}O$ ($\delta^{18}O_{water} = -5.57 \pm 0.1$ ‰), rather only the artificial sediment contained a ^{18}O-label in the form of CHP. The latter was synthesized by dissolving $Ca(H_2PO_4)_2{\cdot}H_2O$ in $H_2^{18}O$ (97 at.% ^{18}O), equilibrating the solution for 30 d at 180 °C, and allowing $CaHPO_4$ to precipitate by evaporation. The pH of the unbuffered solutions was determined before and after the experiments. The initial pH of the FW and FWS solutions was 7.40 ± 0.06 and 7.16 ± 0.06 at 21 °C, respectively, while the pH of the SW solution was 8.04 ± 0.06 at 21 °C (Kral et al., 2021).

Further information on the experimental setup, the composition of the materials used for the experiments, and the structural, chemical, and mineralogical investigations already performed are provided elsewhere (Kral et al., 2021, 2022).

Table 1
Composition of freshwater (FW), seawater (SW), and freshwater plus sediment (FWS) stock solutions [µg/g] (modified after Kral et al., 2022).

	FW	SW	FWS
B^{3+}	2.34 ± 0.06	3.15 ± 0.07	1.79 ± 0.08
Na^{+}	*100.0 ± 0.2*	*10,770 ± 22*	*6.00 ± 0.01*
K^{-}	*100.0 ± 0.2*	*390.0 ± 0.8*	*100.0 ± 0.2*
Ca^{2+}	1,426 ± 15	562 ± 6	197 ± 5
Cl^{-}	*775 ± 2*	*19,350 ± 39*	*600 ± 1*
Mg^{2+}	122.0 ± 1.4	859.2 ± 1.7	67.4 ± 1.5
F^{-}	*5.00 ± 0.01*	*5.00 ± 0.01*	*5.00 ± 0.01*
Sr^{2+}	137.6 ± 0.9	140.1 ± 1.9	122.3 ± 0.2
Zn^{2+}	–	9.6 ± 0.5	–
Fe^{3+}	–	–	In sediment
Lu^{3+}	3.51 ± 0.01	–	2.63 ± 0.15
Nd^{3+}	1.754 ± 0.003	–	0.66 ± 0.02
U^{6+}	16.0 ± 0.2	–	In sediment

The composition of the stock solution constituents B, Ca, Mg, Sr, Zn, Fe, Lu, Nd, and U was determined using a Thermo Scientific Element XR [µg/g ± SD]. The elemental concentration of the remaining elements was calculated from the weight-in and is given in italic font [µg/g ± 0.2 %]. The isotope composition of oxygen was determined using isotope ratio infrared spectroscopy (IRIS). The weighted substances added to all three solutions are B_2O_3, $NaHCO_3$, NaF, KCl, $CaCl_2$, $MgCl_2$, and $SrCl_2$. The FW solution additionally contained $H_2^{18}O$, $NaHCO_3$, $CaCl_2$, $FeCl_3$, $NdCl_3$, $LuCl_3$, and $UO_2(NO_3)_2$. The SW solution comprised $H_2^{18}O$, $NaHCO_3$, $CaCl_2$, NaCl, Na_2SO_4, $Ca(NO_3)_2$, and $ZnCl_2$. The FWS solution also contained $NdCl_3$ and $LuCl_3$. Further substances have been added in the form of artificial sediment (Kral et al., 2021).

2.3. Analytical techniques

2.3.1. Isotope ratio infrared spectroscopy

IRIS analysis was used to determine the isotope composition of oxygen ($\delta^{18}O$) of the experimental solutions (including three solutions from control experiments without CB) and the respective stock solutions. Diluted aliquots of 0.5 µL were analyzed on an L2140-i cavity ring-down spectrometer (Picarro, Inc., Santa Clara, CA, USA). For dilution (≈ 1:200), Milli-Q water (MQ-m) was used ($\delta^{18}O_{MQ\text{-}m} = -8.87 \pm 0.05$ ‰). Laboratory produced reference waters (Chamonix2020, $\delta^{18}O = -14.15$ ‰, Kona2020, $\delta^{18}O = 1.12$ ‰, and Mainztap2020, $\delta^{18}O = -8.78$ ‰) were analyzed in order to normalize the $\delta^{18}O$ values of the samples to the Vienna Standard Mean Ocean Water (VSMOW)-SLAP scale (de Graaf et al., 2021). The 1SD (‰) analytical error of a single oxygen isotope measurement was empirically estimated from multiple measurements.

The repeatability was estimated to be better than ± 0.3 ‰ based on numerous repeat measurements of various solutions. The analytical protocol and information on data calculation are provided by de Graaf

et al., (2020,2021).

2.3.2. Nanoscale secondary ion mass spectrometry

NanoSIMS analyses were performed on one pristine as well as six altered CB samples. A nanoSIMS 50L system (CAMECA, Gennevilliers, France) at the Centre for Microscopy, Characterization and Analysis at the University of Western Australia equipped with a Cs^+ ion beam was used to generate fluorine (^{19}F) and oxygen (^{16}O and ^{18}O) distribution maps of 40 μm x 40 μm large areas along the sample's edge, each measuring 512 pixels x 512 pixels. Strontium (^{88}Sr) and uranium ($^{238}U^{16}O$) maps were recorded using a Hyperion O^- primary ion source. Details on the measurement procedure can be found elsewhere (Kral et al., 2022). The plugin OpenMIMS v3.0.5 (https://nano.bwh.havard.edu) was used in Fiji v1.53c (Schindelin et al., 2012) to generate and process the nanoSIMS images. The linearly-scaled Viridis color palette was used for both color-coding of the ^{18}O and ^{16}O isotope distribution maps and to display modifications of the ^{18}O distribution relative to the ^{16}O distribution in the analyzed areas. The $^{18}O/^{16}O$ value was determined using counts per pixel extracted from the nanoSIMS images. Poisson counting statistics were used to determine the uncertainty of the ^{18}O and ^{16}O counts of each region of interest.

2.3.3. Secondary ion mass spectrometry

The $\delta^{18}O$ profiles of one pristine and three isotopically treated CB samples altered at 90 °C in FW, SW, and FWS solutions for 30 d were obtained using the Potsdam 1280-HR large geometry ion microprobe (CAMECA, Gennevilliers, France). The sample mount was polished to a surface quality of better than 5 μm, was then ultrasonically cleaned in ethanol, and was finally coated with a 35-nm thick gold layer prior to SIMS analysis. A 2.5 nA, 10 keV $^{133}Cs^+$ primary ion beam focused to a ~5 μm diameter spot was used to produce $^{18}O^-$ and $^{16}O^-$ ions. The oxygen ions were simultaneously collected on two Faraday cups over 20 cycles, each lasting 4 s. Based on two apatite reference materials of known chemical and isotope composition (MGMH#128441A and MZ-TH, Wudarska et al., 2022), the measured $^{18}O/^{16}O$ values were corrected for instrumental mass fractionation. A total of ten analyses were performed on the pristine CB and on each of the three altered CB samples. The mean values measured on the two apatite reference materials MGMH#128441A ($\delta^{18}O$ = 9.99 ± 0.56, n = 13) and MZ-TH ($\delta^{18}O$ = 12.55 ± 0.50, n =14) were used for correcting the instrumental mass fractionation using the recommended $\delta^{18}O$ values of these reference materials (Wudarska et al., 2022). The $\delta^{18}O$ values of the unknown are calculated by normalizing their measured $^{18}O/^{16}O$ values relative to the absolute $^{18}O/^{16}O$ zero-point in SMOW ($^{18}O/^{16}O$ = 0.00200520; Baertschi, 1976) via the published values of the apatite reference materials.

2.3.4. Raman spectroscopy

A confocal LabRam HR800 Raman spectrometer at the Institute of Geosciences, University of Bonn, Germany (Horiba Scientific, Palaiseau, France) was used to study structural changes of one pristine and six altered CB samples. Raman spectra were excited with a 200-mW diode-pumped solid-state laser (783.976 nm). The scattered light was detected in the range of 150 to 2,000 cm^{-1} in three spectral windows, each measured 3 x 20 s. These measurements used a 100x objective with a numerical aperture of 0.9. The confocal aperture was set to 1,000 μm and the spectrometer entrance slit was set to 100 μm. A diffraction grating with 600 grooves/mm was used to disperse the polychromatic scattered light onto an electron-multiplier charge-coupled device detector. These settings resulted in a spectral resolution of 1.98 ± 0.03 cm^{-1}, which was empirically estimated from the line width of Ne lines (Table S4). Raman images were acquired at room temperature (21 °C) at the margin and center of the CB samples. The recorded Raman images comprised areas between 41 x 26 μm^2 and 41 x 45 μm^2 in size depending on the individual structure of each sample. The step size was 1 μm, yielding between 1,066 and 1,845 spectra per image. The total acquisition time per single spectrum was *ca.* 200 s. Thus, a single image required between 3 and 4 d to complete.

The first-order band of a pure silicon reference material at 520.7 cm^{-1} was used to calibrate the spectrometer before each measurement. After the measurements, any spectrometer shift was corrected using the 886.19 cm^{-1} line of the laboratory room's ceiling light that was used as an internal standard (Kral et al., 2022). Least-square fitting of an asymmetric Gauss-Lorentz function and a linear background correction in the frequency range between 900 and 1,000 cm^{-1} was performed to determine the frequency of the $\nu_1(PO_4)$ fully symmetrical stretching vibration in apatite (960 cm^{-1}) as well as its life time, given as the full width at half maximum (FWHM) of the $v_1(PO_4)$. The width was corrected for finite slit width effects (Tanabe and Hiraishi, 1980) using the spectral resolution of 1.98 ± 0.03 cm^{-1}. This correction was also applied to all reference data (Table S2) used here for comparison with the spectral resolution specified in the respective publication. For more details about the fitting procedure, the reader is referred to Barthel et al. (2020), Geisler and Menneken (2021), Weber et al. (2021), and Kral et al. (2022).

3. Results

3.1. Oxygen isotope composition of the experimental solutions

Stable oxygen isotope analyses were performed on the stock and experimental solutions (Table 2). The FW and SW stock solutions containing $H_2^{18}O$ yielded $\delta^{18}O$ values of 5,238 ± 66 ‰ and 5,491 ± 79 ‰, respectively. Following the termination of the experiments after 30 d, the $\delta^{18}O$ values of the FW and SW solutions were *ca.* 2 to 3 % and 4 to 5 % lower than their initial value, respectively.

Although the experimental solutions were not buffered, the development of the pH was not very pronounced, probably because the dissolved PO_4 from the sediment and bone acted as a buffer. After 30 d of experiment, the pH of the FW solution slightly increased from 7.04 to 7.68 at 60 °C and to 7.33 at 90 °C. In the FWS solution the pH increased from 7.16 to 7.69 at 60 °C but decreased in the 90 °C experiment to 6.55. In the SW solution, the pH dropped from 8.04 to 7.71 at 60 °C and to 7.42 at 90 °C.

In contrast, the water component of the FWS stock solution was not labeled with $H_2^{18}O$ and had a negative $\delta^{18}O$ value of −5.47 ± 0.04 ‰ (Table 2). In the FWS experiments the only source of enriched ^{18}O was the dissolved PO_4 derived from the isotopically labeled CHP in the sediment. All experimental FWS solutions from the 60 and 90 °C experiments are characterized by $\delta^{18}O$ values that are slightly but statistically significantly higher than those of the stock solution, with the largest changes observed for the 90 °C experiment (Table 2). In addition, FWS control experiments were carried out containing only the FWS

Table 2
Oxygen isotope composition ± 1SD and the shift in $\delta^{18}O$ of freshwater (FW), seawater (SW), and freshwater plus sediment (FWS) stock as well as experimental solutions from experiments terminated after 30 d at 60 and 90 °C determined by isotope ratio infrared spectroscopy (IRIS).

Sample	$\delta^{18}O$ (‰)	± 1SD (‰)	Shift ($\delta^{18}O$) (‰)
FW			
Stock solution	5,238	66	
60 °C	5,120	51	−117
90 °C	5,059	57	−142
SW			
Stock solution	5,491	79	
60 °C	5,255	79	−235
90 °C	5,200	59	−291
FWS			
Stock solution	−5.47	0.04	
60 °C	−4.66	0.04	0.81
60 °C (no CB)	−5.38	0.02	0.09
90 °C	−3.00	0.01	2.47
90 °C (no CB)	−4.30	0.04	1.17

stock solution and the isotopically labeled sediment, but no CB samples. The purpose of these experiments was to determine the interaction between ^{18}O-doped sediment and the stock solution. At 60 °C, no oxygen isotope exchange occurred between ^{18}O-labeled CHP from the sediment and the solution, and only little P (31.77 ± 0.15 µg/g, Kral et al., 2022) was dissolved in the solution. In the 90 °C control experiment, the P concentration increased (293.31 ± 2.74 µg/g, Kral et al., 2022), whereas the $\delta^{18}O$ value increased by only about approximately 1 ‰ (Table 2).

3.2. Oxygen isotope distribution in altered cortical bone

The $^{18}O/^{16}O$ ratios and the respective $\delta^{18}O$ notation of the pristine and altered CB samples extracted from nanoSIMS maps (Fig. 2) are given in Table 3. Note that no attempt was made to correct for instrumental mass fractionation. The average $\delta^{18}O$ value determined from the pristine CB sample is 138.1 with an uncertainty of ± 0.3 ‰, which, however, represents the Poisson counting component only. This value is significantly higher than the average $\delta^{18}O$ value measured using SIMS ($\delta^{18}O_{SMOW} = 0.5 \pm 1.1$ ‰). This high value could be an artifact, perhaps related to the nanoSIMS map region having been rastered over multiple times so as to obtain a better signal. This offset, however, does not affect any conclusion drawn from our data since nanoSIMS was primarily used to spatially visualize the oxygen isotope ratio distribution.

The $\delta^{18}O$ values determined from CB samples exposed to $H_2^{18}O$-containing FW and SW solutions at 60 °C and 90 °C range between −2.6 ± 0.003 ‰ and 362 ± 0.4 ‰ (Table 3). There is no huge difference between the edge and interior of these samples (Fig. 2A-D; Fig. 3A-D). In the rim area, both 60 °C as well as both 90 °C samples were strongly enriched in several other elements originating from the solution, including F (Fig. 2B, D), Sr (Fig. 2C, F), and U (Fig. 2A) - in addition to Zn, Mg, Lu, and Nd as described and discussed in detail in Kral et al. (2022). In the following, this area is referred to as the reaction rim (RR) *sensu* Kral et al. (2021). In contrast, the nanoSIMS $^{18}O/^{16}O$ images of the FWS samples show irregularly, inwardly penetrating ^{18}O-enriched domains (Fig. 2E, F; Fig. 3E, F). Occasionally, the ^{18}O-enriched domains penetrate deeper into the bone along microcracks (Fig. 2E, F). The average $\delta^{18}O$ calculated from the RR of the 60 °C FWS sample is 2,286 ± 4 ‰. Even 30 µm away from the edge the average $\delta^{18}O$ is still higher than the ratios measured in the pristine sample (Fig. 3E). In the 90 °C FWS sample, the ^{18}O enrichment was even more pronounced in the RR

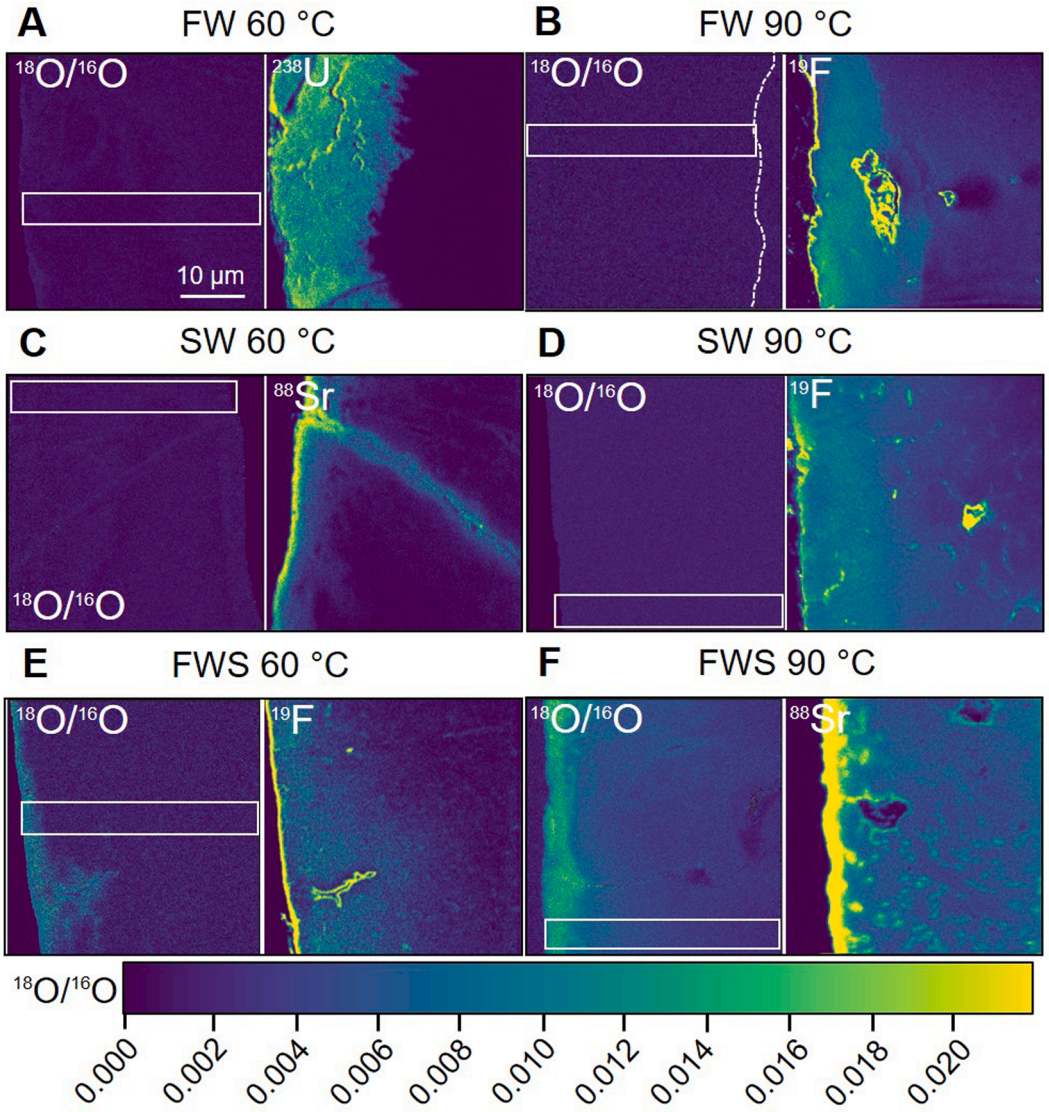

Fig. 2. Isotope ratio and element distribution images obtained by nanoSIMS of CB samples reacted at 60 and 90 °C for 30 d in FW **(A, B)**, SW **(C, D)**, and FWS solutions containing ^{18}O-enriched CHP **(E, F)**. The images display the isotopic ratio of oxygen at each pixel (0.078 µm) obtained by dividing the ^{16}O and ^{18}O counts of each pixel compared to the isotope distribution of ^{238}U **(A)**, ^{19}F **(B)**, ^{88}Sr **(C)**, ^{19}F **(D)**, ^{19}F **(E)**, and ^{88}Sr **(F)**. The white boxes mark the regions from which nanoSIMS $^{18}O/^{16}O$ profiles were extracted (see Fig. 3, Table S1). The field of view of each image is 40 x 40 µm^2.

Table 3
$^{18}O/^{16}O$ ratios with an 1SD uncertainty and the respective $\delta^{18}O$ value ± 1SD (‰) of the inner parts and the reaction rim (RR), obtained from nanoSIMS oxygen isotope distribution images.

	Interior				Reaction rim			
Sample	No. of pixels	$^{18}O/^{16}O_{avg}$	$\delta^{18}O$ (‰)	± 1SD* (‰)	No. of pixels	$^{18}O/^{16}O_{RR}$	$\delta^{18}O$ (‰)	± 1SD* (‰)
Pristine	262,144	0.002305(55)	138.1	0.3				
FW, 60 °C	261,121	0.002759(30)	362.4	0.4				
FW, 90 °C	262,144	0.002549(31)	258.8	0.3				
SW, 60 °C	198,136	0.002020(26)	−2.6	0.003				
SW, 90 °C	262,144	0.002390(22)	180.1	0.2				
FWS, 60 °C	247,454	0.005267(95)	1,600.9	2.9	60,805	0.0066(12)	2,286.0	4.3
FWS, 90 °C	242,176	0.006065(47)	1,994.6	1.5	19,968	0.0129(27)	5,387.7	11.3

* Internal uncertainties were estimated from the total ^{18}O and ^{16}O counts obtained from the nanoSIMS images and determined using Poisson counting statistics. $^{18}O/^{16}O_{RR}$ gives the mean oxygen isotope ratio only in the RR of the FWS samples.

(5,388 ± 11 ‰) and 30 μm away from the edge (1,995 ± 2 ‰) of the sample (Fig. 2F; Fig. 3F). It is noteworthy that the F enrichment correlates well with the observed ^{18}O enrichment (Fig. 2E).

3.3. Changes of oxygen isotope composition in altered cortical bone samples

Large geometry SIMS measurements were performed on one pristine (control) and three altered (SW, FW, and FWS) CB samples from experiments that ran 30 d at 90 °C. For the altered CB samples, five analyses were performed laterally displaced along the sample's edge with one analysis every 500 μm and another five analyses over a distance of up to 1,000 μm toward the interior with one analysis every 200 μm (Table 4). The measurements revealed an average $\delta^{18}O_{SMOW}$ value of 0.5 ± 1.1 ‰ (≙ $^{18}O/^{16}O = 0.002006$) in the pristine sample.

Analyses of the 90 °C FWS CB sample showed a strong enrichment with ^{18}O in the RR ($\delta^{18}O_{max} = 2{,}925$ ‰) but while still retaining values comparable to the pristine CB sample further inward - both are consistent with the nanoSIMS results. Interestingly, in the 90 °C SW CB sample, both SIMS profiles, the one parallel to the sample edge and the other one running 1,000 μm toward the sample interior, with one analysis every 200 μm, showed that the sample was consistently enriched with ^{18}O ($\delta^{18}O_{avg} = 290 \pm 29$ ‰, Table 4), which, at least in the outermost 40 μm, is consistent with the nanoSIMS results (Fig. 3). The 90 °C FW sample also showed a consistent enrichment with ^{18}O from the edge toward the sample's interior ($\delta^{18}O_{avg} = 347 \pm 17$ ‰, Table 4).

3.4. Mineralogical features of altered bioapatite

Raman spectroscopy was used to assess possible mineralogical changes associated with the experimental treatment of the CB samples. The bandwidth Γ, given as the full width at half maximum (FWHM), and the frequency (ν) of the $\nu_1(PO_4)$ fully symmetric stretching band are two parameters that have previously been used to obtain information on the mineralogical composition and crystal structure of bioapatite (Thomas et al., 2011; Dal Sasso et al., 2018; Barthel et al., 2020; Weber et al., 2021; Kral et al., 2022). Fig. 4 shows a plot of both parameters from the experimentally altered CB samples and reference data from various sources (Table S2). Data from the RR and interior of CB samples altered in FW and SW solutions were adapted from Kral et al. (2022) (Table S3).

The Raman spectral parameters from the pristine CB sample (n = 92 spectra) show a significant variability due to the natural heterogeneity of the CB sample; the $\nu_1(PO_4)$ band position ranges from 960.7 to 961.4 cm^{-1} with an average value of 961.0 ± 0.1 cm^{-1}, and the FWHM lies between 13.4 and 15.0 cm^{-1} with an average value of 14.1 ± 0.3 cm^{-1} (Fig. 4). The 95 % confidence limit of the data distribution is given in the diagram by a green ellipse. The long axis of the ellipse, representing the reduced major axis regression, has a slope $d\nu/d\Gamma$ of −0.40 and, as such, points to the position of magmatic FAp (Trend II). It is noteworthy that the reduced major axis slope agrees very well with the slopes observed for both modern and fluoridated fossil lizard bones (Barthel et al., 2020). By looking at the frequency versus bandwidth relationship for the RR data of the CB samples altered for 30 d at 90 °C (colored in yellow and red), it is instantly apparent that in all experiments the nano-crystalline bioapatite matrix must have been significantly altered, which is reflected by a clear shift of the $\nu_1(PO_4)$ band to higher frequencies (wavenumbers) and partly to lower bandwidths compared to the data from pristine CB.

The RR data from the 90 °C FWS CB samples (solid red triangles, n = 1,139 spectra) define a broad trend that evolves toward higher frequencies and decreasing bandwidths. Towards lower frequencies, the spread of the data is delimited by Trend II (Fig. 4), that connects pristine bioapatite and magmatic FAp. The data obtained from the RR of the 90 °C CB samples (solid yellow squares, n = 405) and FW experiments (solid yellow circles, n = 450) evolve toward higher frequencies but not toward decreasing bandwidths. It appears that the data from experiments without sediment (FW, SW) and some data points from the 90 °C experiment with sediment (FWS) follow a steeper linear array with a slope $d\nu/d\Gamma$ of about −1.2 (Trend III) that runs parallel to the trend defined by horse dentin that had experimentally been fluoridated in NaF solution (Fig. 4; Pasteris and Ding, 2009). In contrast, the RR data from the 90 °C FW sample show a shift toward higher frequencies but with a significant overlap with data from the pristine sample (Kral et al., 2022). The reduced major axis slope, i.e., the orientation of the long axis of the confidence ellipse, is similar to that given by Trend III. The Raman frequencies of the $\nu_1(PO_4)$ mode obtained from the RR of the SW sample are distinctly higher than those from the pristine sample. In contrast the average $\nu_1(PO_4)$ bandwidth shows only a slight decrease. The respective 95 % confidence ellipse is oriented almost parallel to those of the pristine sample. A similar picture emerges for the RR data from the 60 °C FW sample (Kral et al., 2022). However, these data are characterized by an even larger bandwidth, on average, than that of pristine CB, resulting in a positive slope tie-line between pristine and altered CB on the frequency-versus-width plot.

As with the FW and SW samples, Raman spectra were also collected from the interior of the FWS sample. The data points of the FWS sample show a different pattern than those of the FW and SW samples, which show a linear trend toward well-ordered nano-crystalline HAp (Trend I), i.e., decreasing bandwidth but only slightly increasing frequency (961.0 to 961.5 cm^{-1}). The frequency from the interior of the FWS sample are distinctly increased in one group, ranging from 962 to 963 cm^{-1}, while the bandwidth from all FWS data does not vary much around an average of 12 cm^{-1}. Data from this measurement were obtained from an intersect from the interior towards the sample's edge and clearly show the effect of fluorine-incorporation. In contrast, data from a second measurement plot at similar frequencies and bandwidth as the FW and SW data, following Trend I.

4. Discussion

For fossilization to occur, the *post mortem* bone must be rapidly transformed into a more stable form that is less susceptible to diagenetic

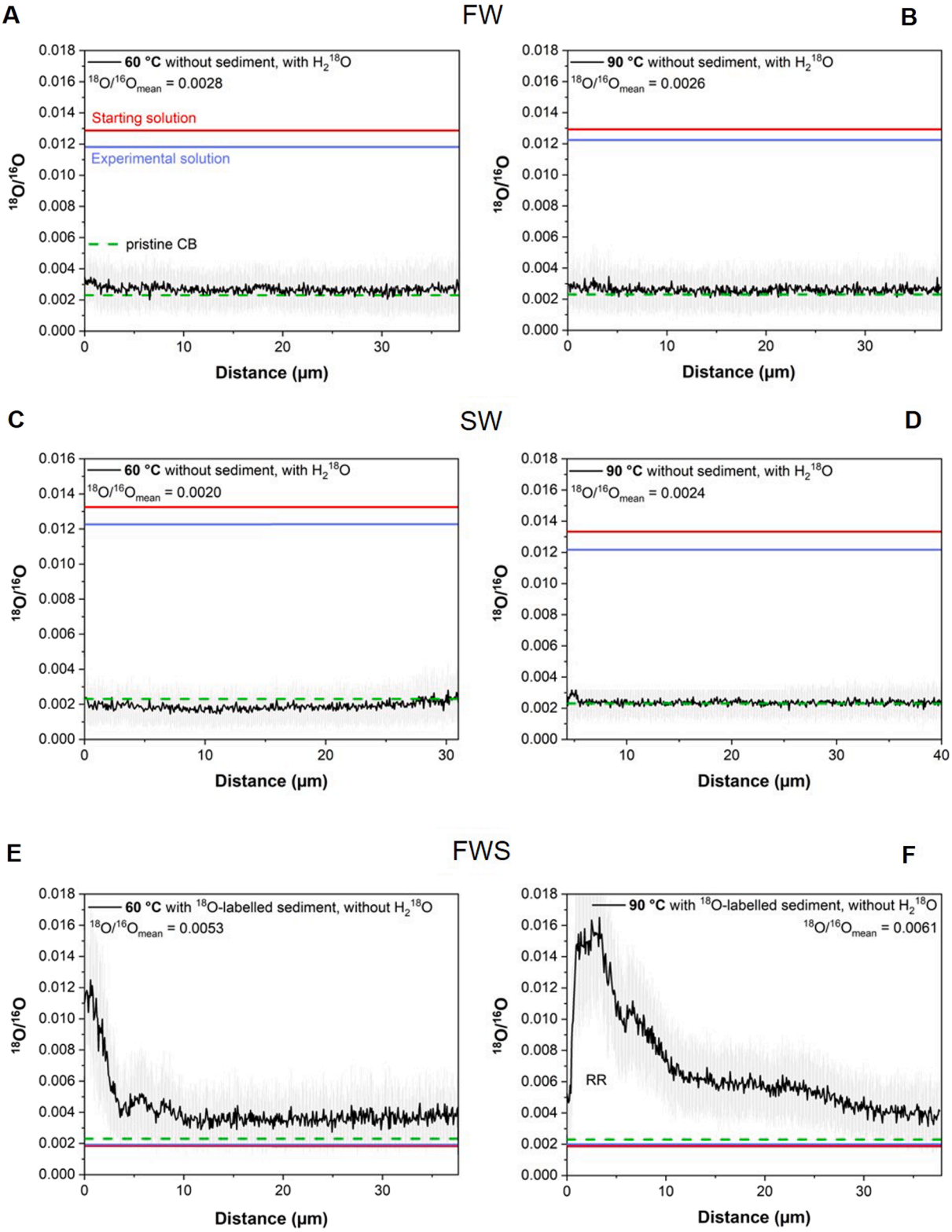

Fig. 3. NanoSIMS $^{18}O/^{16}O$ profiles of the FW, SW, and FWS CB samples across the transects shown in Fig. 2. The $^{18}O/^{16}O$ profiles illustrate the $^{18}O/^{16}O$ ratio of FW (A, B), SW (C, D), and FWS (E, F) CB samples from the sample's edge toward the interior. The $^{18}O/^{16}O$ profiles were derived by summing the ions observed from the white boxes in Fig. 2. Note, that the epoxy parts of the profile were not considered in the diagrams. The lateral resolution was approximately 100 nm. The dashed green line marks the $^{18}O/^{16}O$ value of the pristine CB sample, while the straight red and blue lines display the stable oxygen isotope composition of the starting solution and the experimental solution after terminating the experiments, respectively. The underlying data are provided in Table S1.

Table 4
SIMS oxygen isotope compositions ($\delta^{18}O$) at ten different spots measured along a ≈ 1 mm profile from the margin towards the center of the CB sample on one unaltered control and the 30 d, 90 °C CB samples from FW, SW, and FWS experiments.

	Oxygen isotope data ($\delta^{18}O$, ‰, SMOW)									
Sample	**1**	**2**	**3**	**4**	**5**	**6**	**7**	**8**	**9**	**10**
Control	*−24.3*	−0.2	2.4	1.5	−0.6	*16.0*	0.5	1.5	−1.0	−0.2
SW	276.8	321.6	287.1	276.3	256.3	295.1	357.3	257.7	286.3	287.9
FW	344.5	324.6	323.4	360.0	369.8	358.6	328.0	357.3	336.7	366.8
FWS	2,925.5	2,369.7	135.9	140.5	749.3	−1.01	0.10	−2.75	−2.07	2.09

Italic values are considered as outliers and were not used for calculations due to low counting statistics. SMOW = Standard Mean Ocean Water.

change, thus preventing the bone from decaying (e.g., Berna et al., 2004). During the fossilization process, both collagen and bioapatite must be replaced with thermodynamically more stable apatite (Hinz and Kohn, 2010). However, this requires uptake and incorporation of additional material, in particular Ca and P – in nature, the latter is usually available in the form of aqueous PO_4^{3-}. To understand the underlying mechanisms during bone fossilization, ^{18}O was used as a tracer that would distinguish between recrystallization (i.e., interface-coupled dissolution-precipitation) of bioapatite and mineralization of bone tissue with new apatite (from externally derived aqueous Ca and PO_4). This experimental approach is possible because at Earth surface temperatures, PO_4 is transferred from sediment or ambient (pore) water into bone with only small oxygen isotope fractionation occurring (≈ +1 ‰, Liang and Blake, 2007). Thus, PO_4 should preserve its initial oxygen isotope composition ($\delta^{18}O_{PO4}$), which can then be used as a source tracer for the PO_4 group. Furthermore, by using either ^{18}O-enriched water or an ^{18}O-enriched sedimentary PO_4 source, an investigation of how the environmental oxygen uptake in the presence or absence of an external PO_4 source takes place is possible.

4.1. Alteration of the mineral phase

Our Raman spectra did not provide any evidence for the formation of new mineral phases other than apatite in the altered CB samples. However, the relationship between the frequency and bandwidth of the v_1 mode of PO_4 indicates that significant crystallographic changes of the bioapatite must have occurred (Fig. 4). From a physical perspective, the frequency and lifetime (represented by the bandwidth) of an excited atomic vibration in a disordered, nano-crystalline solid solution such as bioapatite are expected to have a negative linear correlation. At the same time, the absolute values and the slope depend on structural properties such as defect density, substitution mismatch, and/or crystallite size. When interpreting the Raman data from bone material, however, it should be kept in mind that due to the nano-crystalline nature of the apatite phase(s), a Raman spectrum represents a mixed spectrum from thousands of nano-crystallites and consequently average Raman parameters.

In a F-free solution, modification of bioapatite through dissolution-precipitation processes should lead to a trend toward stoichiometric, pure nano-crystalline HAp, while in an F-bearing solution, FAp would be favored (Aufort et al., 2019). For example, Weber et al. (2021) observed a trend toward pure HAp in modern elephant dentin altered for up to 63 d at 30 and 90 °C in a nominally F-free, strongly acidic solution (Fig. 4). Some Raman data from reacted dentin show a linear trend with a relatively flat $d\nu/d\Gamma$ slope of about −0.14 (Trend I) before kinking toward higher frequencies. The authors explained the observed kink away from Trend I toward higher frequencies by the release of F from the Teflon© reactor at higher temperatures and longer experiment durations, leading to the increased formation of a F-bearing apatite phase. Incorporating F leads to a shorter average P–O bond length which is reflected by a higher $v_1(PO_4)$ frequency (e.g., Penel et al., 1997; Lanfranco et al., 2003; Thomas et al., 2007, 2011).

The starting pH of the unbuffered aqueous solutions used in our study was 6 to 7 pH units higher than in the alteration experiments of dental cubes by Weber et al. (2021) and remained relatively stable over time. Therefore, we assumed that the alteration effects on the CB samples, which is more susceptible to alteration than tooth enamel, were less pronounced. All solutions had a pH ranging from neutral to slightly alkaline. During the experiments, the pH value remained within the roughly defined range of the so-called recrystallization window, in which conditions prevail that promote apatite replacement reactions and impede large-scale apatite dissolution (Berna et al., 2004). The CB samples showed indeed less alteration effects compared to Weber et al. (2021), but similar observations were made, including the formation of pure, nano-crystalline HAp and FAp. Kral et al. (2022) showed that CO_3-poor or even CO_3-free HAp partly replaced the bioapatite in the center of CB samples from the 90 °C FW and SW experiments. This was accompanied by a depletion in Ca and P in the RR, which was also observed in an earlier study by Turner-Walker (2011). This suggests that a redistribution of Ca and P (in the form of PO_4) from the RR toward the interior of the CB samples must have occurred through a spatially-uncoupled dissolution-precipitation process. Initially, F was present in all three solutions with a concentration of 5 mg/L, potentially allowing for the precipitation of FAp, which according to Aufort et al. (2019) should preferentially form relative to HAp. However, using nanoSIMS in conjunction with electron microprobe analysis (EMPA) imaging, Kral et al. (2022) showed that in the FW and SW samples only the RR was enriched in F (Fig. 2B, D, E), while in the FWS sample F was also detected around canal structures within the CB (Fig. S1). Indeed, the observed shift of the $\nu_1(PO_4)$ mode frequency to higher values clearly indicates the formation of new FAp in the FWS sample. It follows that for the interior of the FW and SW CB samples, the conditions for the formation of stoichiometric nano-crystalline HAp were present and uncoupled from the formation of a F-bearing apatite phase in the RR.

The frequency shift observed in the RR data is accompanied by only a slight reduction of the measured bandwidth, which has also been observed for *in situ* monitored fluoridation of horse dentin (Pasteris and Ding, 2009). These and other authors (Ren et al., 2019) have suggested that fluoridation occurred by an interface-coupled dissolution-precipitation process during which bioapatite nano-crystallites partially dissolved stoichiometrically and released Ca and PO_4 to the F-bearing solution, which caused the supersaturation and precipitation of a FAp-HAp solid solution from an interface fluid film, gradually replacing the bioapatite pseudomorphically. Such a process would be thermodynamically driven by the difference in solubility between bioapatite and highly insoluble FAp (Zhu et al., 2009; Qiao et al., 2017). The formation of several nanometer-thick surface layers of FAp on bulk HAp has indeed been observed experimentally, but this was attributed to kinetically-controlled diffusion of F from the HAp surface into the crystal (Lin et al., 1981; Müller et al., 2010) or explained as the result of an adsorption mechanism (e.g., Sternitzke et al., 2012; Mosiman et al., 2021). However, many solid solution-aqueous solution processes such as interface-coupled replacement, have been shown to be favored over diffusion-controlled processes, particularly at low temperatures (Putnis, 2002; Prieto, 2009; Putnis et al., 2009; Ruiz-Agudo et al., 2014). In any case, the fluoridation process leads to the formation of a composite material on the nanoscale with an F-rich rim and a bioapatite core. It is conceivable that the new interface formed between the two nano-

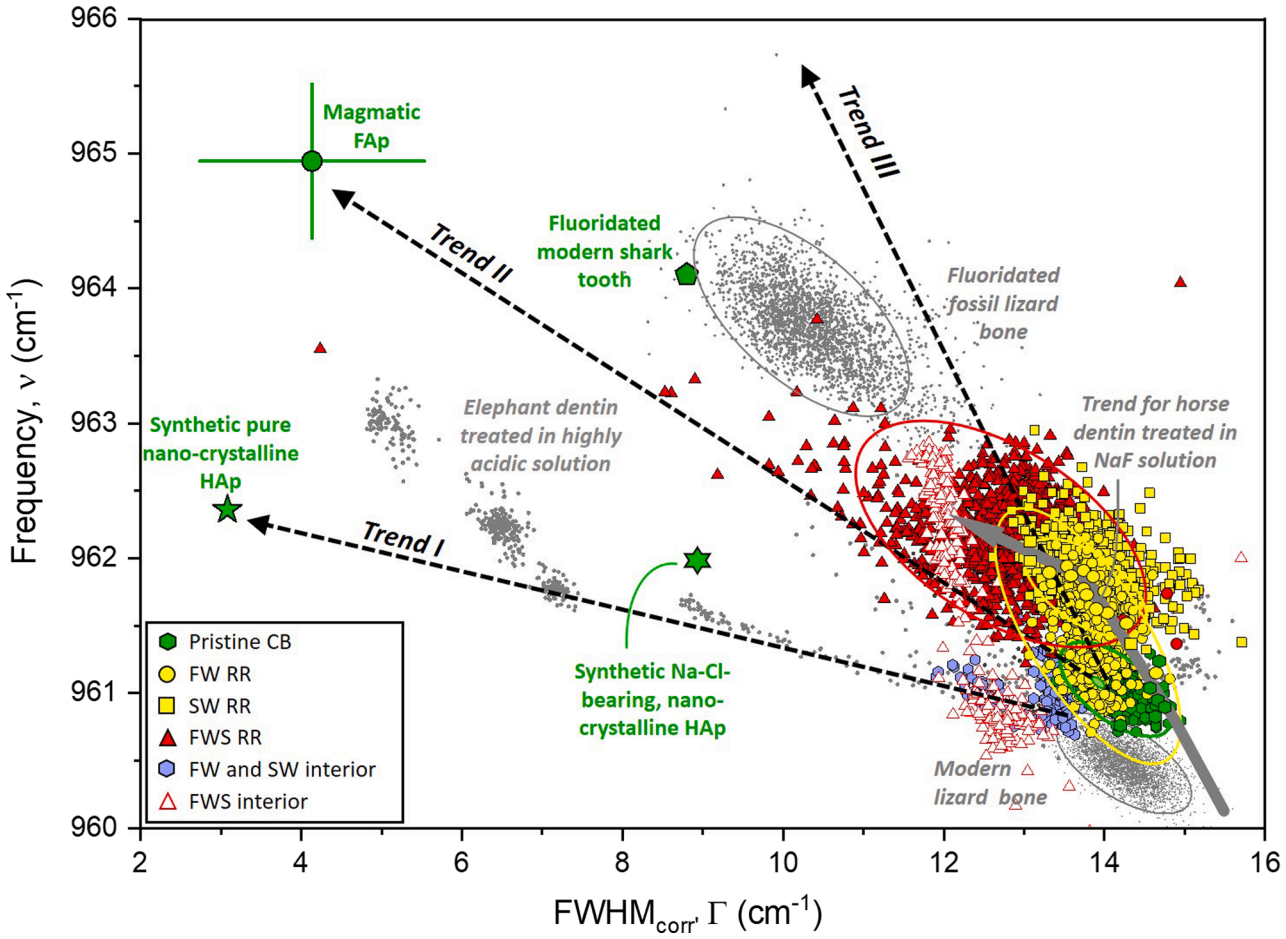

Fig. 4. Plot of Raman spectral parameters. The frequency, ν of the $\nu_1(PO_4)$ band of pristine and the RR as well as the interior of altered CB samples as a function of its bandwidth, Γ compared to various reference data (Table S2–S4): pristine and altered FW and SW CB samples (Kral et al., 2022), modern and fluoridated fossil lizard bone (Barthel et al., 2020), modern fluoridated shark tooth and the trend for horse dentin (Pasteris and Ding, 2009), magmatic FAp and elephant dentin HAp (Weber et al., 2021), synthetic nano-crystalline, stoichiometric HAp (Asjadi et al., 2019), and synthetic nano-crystalline, Na- and Cl-bearing HAp (Thomas et al., 2011). The altered CB samples were derived from experiments conducted at 90 °C for 30 d in FW, SW, or FWS solution.

crystalline apatite phases may cause additional band broadening; this broadening should decrease once FAp fully replaces the original bioapatite nano-crystallites. In fact, the kink of the fluoridation trend for horse dentin toward a decreasing bandwidth (Fig. 4) may be explained by a complete replacement of bioapatite by FAp. Whereas the RR data from experiments conducted without sediment follow the steeply-sloped Trend III, the data from the RR of the FWS samples that reacted with PO_4-delivering sediment seem to split into two groups (solid red triangles in Fig. 4). Therefore, it is reasonable to link these two groups (Trends II and III) to (i) variable fractions of a newly crystallized, nano-crystalline and F-bearing apatite and (ii) recrystallized and thereby fluoridated nano-crystalline bioapatite. Interestingly, Raman data from the interior of the FWS sample which were obtained from an intersect between the interior and the rim followed Trend III, i.e., the frequency increased, while the bandwidth decreased to ~12 cm^{-1}- indicative of the formation of CO_3-poor FAp. Data from a second measurement, only from the interior of the FWS sample follow Trend I, which connects pristine CB and synthetic HAp.

4.2. *Distinguishing between recrystallization and mineralization*

Most of the original bioapatite in fossil bone is usually replaced by a secondary, more stable apatite phase, generally CO_3-FAp (Hubert et al., 1996; Berna et al., 2004; Trueman et al., 2004; Piga et al., 2016). It is widely assumed that bone recrystallization and mineralization occur during the early stages of fossilization (Nielsen-Marsh and Hedges, 2000; Trueman et al., 2004, 2008; Kohn, 2008). However, it is still unclear how soon bone recrystallization begins *post mortem* and what the specific processes are, e.g., diffusional ionic exchange, surface adsorption, and spatially-uncoupled or interface-coupled dissolution-precipitation (Kelly and Bassingthwaighte, 1977; Fernández-Seara et al., 2002; Trueman et al., 2008; Kohn and Moses, 2013; Keenan and Engel, 2017; Konrad-Schmolke et al., 2018; Renard et al., 2019). Therefore, it still remains to be established which of the different mechanisms actually lead to the fossilization of bone.

Based on both the Raman and EMP data from a previous study (Kral et al., 2022), we suggest here that at the beginning of the reaction spatially-uncoupled dissolution-precipitation processes have led to a redistribution of Ca and P (in the form of PO_4) from the RR to the interior of the altered CB samples. Pure HAp precipitated in the interior of FW and SW samples, while CO_3-FAp formed in the interior of the FWS sample. In this scenario, neither spatially-uncoupled nor interface-coupled dissolution-precipitation processes would significantly alter the oxygen isotope composition because the residence time of a PO_4 molecule in solution at the reaction interface is expected to be too short for significant oxygen isotope exchange.

PO_4 is a relatively inert molecule due to its strong P–O bonds. In the PO_4-H_2O system, the O-exchange is high only under rather extreme conditions such as low pH (< 3) or high temperatures (> 115 °C) (Lécuyer et al., 1999; O'Neil et al., 2003; Chang et al., 2021), which are not typical for early diagenetic settings. Although O-exchange rates increase with increasing temperature, experiments have shown that even

at 70–180 °C, measurable O-exchange occurred only after months (Lécuyer et al., 1999; O'Neil et al., 2003; Chang et al., 2021). Therefore, it is assumed that under the present experimental conditions (i.e., 60 and 90 °C, 30 d experimental duration, neutral to slightly alkaline pH), little exchange between the oxygen atoms in the PO_4 molecules from dissolved bioapatite and the ^{18}O from the aqueous FW and SW solution will occur. We recall that the same is reasonable for the reverse reaction in the FWS experimental series, i.e., there will be little to no exchange of oxygen atoms between aqueous phosphate from dissolved sedimentary ^{18}O-doped CHP and oxygen atoms in H_2O. This is also reflected by the observed limited changes of the oxygen isotope composition of the aqueous solution at the end of the experiment (Table 2).

For the FW and SW samples, at first glance, the assumption of limited O-exchange seems contradictory, since the SIMS analyses revealed an enrichment with ^{18}O even 1,000 μm away from the edge of these samples (Table 4). However, since the $\delta^{18}O$ values remain at a similar level of *ca.* 300 ‰ from the RR toward the center of the sample, it is assumed that $H_2^{18}O$ was distributed via the cortical canal network (Kral et al., 2021, 2022) and was adsorptively bound to bioapatite crystallite surfaces and/or to collagen peptide chains rather than incorporated into the mineral phase. Vaissier Welborn (2021) showed experimentally that the ability of HAp to adsorb water is generally high in presence of collagen and about 30 % higher when collagen still maintains its original triple-helix structure. Thus, the water adsorption properties of HAp are directly related to the degree of collagen degradation.

Strong enrichment of ^{18}O was observed only in the RR of the CB samples immersed in the FWS solution together with artificial sediment containing ^{18}O-doped CHP (Fig. 2E; Fig. 3A, B). SIMS analyses revealed $\delta^{18}O$ values of 2,916 ‰ (Table 4) for the RR of the 90 °C FWS sample, while values similar to those in the pristine sample ($\delta^{18}O_{avg} = 0.50$ ‰) were measured at the same sample's interior (Table 4). It follows that in the interior of FWS samples CO_3-FAp recrystallized, which would not affect the oxygen isotope composition. In contrast, the observed ^{18}O enrichment in the RR of CB from the FWS experiments combined with the presence of CO_3-free FAp is evidence for the mineralization of CB through newly grown authigenic FAp. The latter must have incorporated ^{18}O-enriched PO_4 from the ambient fluid derived from the CHP contained within the sediment.

External PO_4 present in the embedding sedimentary environment can originate from either a biotic or abiotic source. Most likely it is present as an already dissolved ion in the diagenetic fluid, e.g., from already decomposed remains of the same (or another) vertebrate organism. Although PO_4 can also be present in solid form in the sediment, e.g., as detrital apatite (Filippelli, 2002), due to its lower solubility compared to biogenic apatite (Oxmann and Schwendenmann, 2014) it is unlikely to be a relevant source of external PO_4. The PO_4 content in marine or terrestrial sediments is site-specific and varies between a few μg/g up to several thousand μg/g. For example, Mesozoic sediments from the Eastern Indian Ocean show relatively similar phosphate contents (1,000 μg/g) at different sampling sites, while greater variations were found in Cenozoic sediments with a mean content of 1,530 μg/g and maximum value of approximately 5,000 μg/g (Cook, 1973). In marine sediments the PO_4 content depends on several factors, such as the organic matter sources, primary productivity in waters at site of deposition, or how much Fe is in the water column that could bind and scavenge PO_4. More specifically, for nearshore marine as well as astuarine sediments, the amount, composition, and condition of the sedimentary input are also relevant factors. It is, therefore, difficult to predict the amount of PO_4 present and available for incorporation during fossilization. Nevertheless, the present study unambiguously shows that when external PO_4 is present in a dissolvable form, its incorporation occurs rapidly, resulting in accelerated bone fossilization which increases the chance of preservation. Moreover, the oxygen isotope composition is altered rapidly due to the formation of newly grown secondary apatite, at least in the RR. Such RRs with altered oxygen isotope compositions have for instance been documented in Late Pleistocene terrestrial mammal bones from the North Sea that were fossilized in a marine setting (Tütken et al., 2008).

Despite considerable research having been invested towards distinguishing between original and diagenetically modified oxygen isotope compositions (Iacumin et al., 1996, 2022; Blake et al., 1997; Zazzo et al., 2004; Tütken et al., 2008; Gehler et al., 2011; Thomas et al., 2011; Lécuyer and Flandrois, 2023), the underlying processes are not yet fully understood. In a previous study, the oxygen isotope exchange between $(PO_4)_{aq}$ and H_2O as well as the compositional stability of the CO_3 ($\delta^{13}C$, $\delta^{18}O_c$) and PO_4 ($\delta^{18}O_P$) group in bioapatite were investigated under biotic and abiotic conditions by exposing bone and tooth enamel powders to ^{13}C- and ^{18}O-labeled aqueous solutions (Zazzo et al., 2004). It was found that chemical alteration, i.e., rapid incorporation of ^{13}C and ^{18}O into bioapatite either by oxygen exchange or by the formation of secondary minerals, already starts a few days *post mortem*, even before structural modifications become apparent. Under inorganic conditions, PO_4 appeared to be more resistant to oxygen isotope exchange with water than CO_3, which was reversed in the presence of microbes that provide enzymes catalyzing PO_4 bond cleavage, thereby enhancing oxygen isotope exchange with water. Zazzo and colleagues suggested that such exchange reactions also occur in nature within a few days *post mortem*, which basically agrees with the experimental observation that chemical modifications of bone start well before changes in its histology occur (Kral et al., 2021, 2022).

The data from our study can, however, only partially confirm Zazzo et al.'s (2004) observation that large amounts of ^{13}C and ^{18}O are incorporated into the bioapatite during their experiments. In the present study, it has been shown that the oxygen exchange between dissolved ^{18}O-doped PO_4 (derived from a sediment CHP source) and the water in our FWS solution ($\delta^{18}O_{FWS} = -5.47 \pm 0.10$ ‰) was insignificant even after 30 d at 90 °C ($\Delta\delta^{18}O_{60°C} = 0.09$ ‰, $\Delta\delta^{18}O_{90°C} = 1.17$ ‰, Table 2). Likewise, no significant oxygen exchange between ^{18}O-doped water and bioapatite could be detected in either the FW or the SW experiments. The changes in $\delta^{18}O$ of the FW and SW solutions correspond to the slightly increasing $\delta^{18}O$ values in the respective CB samples measured using SIMS. The enrichment in ^{18}O is not nearly as high as in the experiments with sediment containing ^{18}O-enriched CHP. This is because PO_4 is initially released during the congruent dissolution of bioapatite and then reprecipitated as new, possibly CO_3-bearing FAp along an inwardly migrating replacement front, producing pseudomorphs of the original nano-crystallites. In such a process, the residence time of PO_4 released by apatite dissolution into the interface solution as well as the time for abiotic oxygen isotope exchange is very short, since it is immediately reprecipitated as new apatite replacing the bioapatite crystallites.

The observation that in the FW and SW samples ^{18}O is enriched (~ 300 ‰) throughout the sample from its edge to the interior, although they are characterized by chemical a RR, indicates that the observed recrystallization of the bioapatite nano-crystals in the RR (likely by an interface-coupled dissolution-precipitation process) is not associated with a significant oxygen isotope exchange between the ^{18}O-doped solution and the apatite. The ^{18}O enrichment in the CB samples can be explained by the adsorption of ^{18}OH to HAp and CO_3-bearing HAp surfaces derived from H_2O molecules which can dissociate spontaneously to OH^- (Peccati et al., 2018). It is likely that these hydroxyl-ions will be incorporated into the crystal lattice over time either by interface-coupled dissolution-precipitation or by the formation of a new apatite phase.

An explanation for the different results may be that Zazzo et al. (2004) used bone and tooth enamel powders, while Kral et al. (2021, 2022) used intact CB samples. Powders have a much larger surface area than intact bone samples, which for surface-driven processes increases the reaction rate. The extent of the change in abiotic oxygen isotope composition is influenced by the type of mineral replacement process. Under the assumption that the residence time of the PO_4 from the dissolving bone apatite in the solution is short as compared to the kinetics

of abiotic oxygen isotope exchange between PO_4 and water, during an interface-coupled dissolution-precipitation process, the oxygen isotope composition should change only slightly. If, on the other hand, new apatite is formed, the average $\delta^{18}O$ value could change more substantially. In this case, however, the absolute change in ^{18}O content depends on the difference in the oxygen isotope composition between bone and external phosphate and, of course, on the proportion of external PO_4 added to the fossil. Another process, which may have changed the average ^{18}O composition, is the dissociation of $H_2^{18}O$ to $^{18}OH^-$, which binds adsorptively to the crystallite surface (Peccati et al., 2018). The incorporation of these ions into the crystal lattice is slow in the presence of F^-, because the formation of HAp is less favorable than FAp, which correlates with our data showing no difference in ^{18}O composition between areas in the CB samples with newly precipitated FAp and reprecipitated HAp (Table 4). Even though the average oxygen isotope composition of bone is influenced over time by this process, it has no influence on the oxygen isotope composition of PO_4.

5. Conclusion

This experimental ^{18}O tracer study demonstrates that the presence or absence of a sedimentary PO_4 source strongly influences *post mortem* bone mineralization and alteration, thus the likelihood of fossilization. Both uncoupled and interface-coupled dissolution and precipitation processes occurred in the CB samples from experiments without an external PO_4 source. This resulted in a spatially restricted and distinct transformation of bioapatite into CO_3-bearing FAp in the RR and CO_3-deficient HAp in the interior of the samples. In this scenario, the porous CB samples absorbed the ^{18}O-enriched fluid like a sponge, and $H_2^{18}O$ became bound to bone matrix, resulting in a weak but uniform enrichment with ^{18}O throughout the samples. The oxygen isotope composition was altered within a few weeks (under heat-accelerated conditions). This isotope shift may not be permanent, as $H_2^{18}O$ was presumably mainly adsorptively bound to bioapatite crystallites making it vulnerable to return to the solution when the crystallites dissolve. Thus, when fossil bone is derived from a diagenetic environment without a PO_4 source, the oxygen isotope composition is influenced by that of the diagenetic fluid, implying that the oxygen isotope composition is rather representative of a later stage of the early diagenetic phase. In contrast, the presence of a sedimentary PO_4 source led to rapid mineralization by FAp in the RR, as well as a change in the oxygen isotope composition through the incorporation of external PO_4. Sediment-derived ^{18}O-doped PO_4 was dissolved, transported into the bone via the fluid, and was incorporated very rapidly, as indicated by high $\delta^{18}O$ values in the RR. At the same time, CO_3-bearing FAp - which was not enriched with ^{18}O - precipitated in the sample's interior. Consequently, the incorporation of external PO_4 may lead to a fast modification of the oxygen isotope composition of the bone mineral phase, such that a mixture of primarily and secondarily incorporated PO_4 determines the $\delta^{18}O_{PO4}$ value in the RR (after prolonged diagenetic alteration possibly throughout the entire bone), while in the interior the original oxygen isotope composition of CB remains unchanged during at least the first weeks, months or potentially years *post mortem*. Therefore, if an external PO_4 source is present shortly after death, bone fossilization is accelerated and the oxygen isotope composition, at least of the outer parts of the bone, is more readily altered by the earliest stages of the fossilization process.

Credit authorship contribution statement

Anna G. Kral: Writing – original draft, review & editing, Conceptualization, Methodology, Formal analysis. **Thorsten Geisler:** Writing – review & editing, Supervision, Funding acquisition, Conceptualization. **Michael Wiedenbeck:** Writing – review & editing, Methodology, Formal analysis. **Paul Guagliardo:** Methodology. **Thomas Tütken:** Writing – review & editing, Supervision, Funding acquisition, Formal analysis, Conceptualization.

Declaration of competing interest

The authors declare that they have no known competing financial interests or personal relationships that could have appeared to influence the work reported in this paper.

Acknowledgments

We thank Hubert Vonhof for performing the water oxygen isotope analyses and Jennifer Leichliter for helping with the water sample preparation. Frédéric Couffignal is acknowledged for performing the large geometry SIMS analysis. Alexander Ziegler is thanked for discussions and comments on the manuscript. This work was made possible in part by the OpenMIMS software, whose development was funded by the National Resource for Imaging Mass Spectrometry (NIH/NIBIB 5P41 EB001974-10). Funding for this study was provided by the Deutsche Forschungsgemeinschaft through grants GE 1094/23-1 and INST 217/1010-1 to TG as well as grant TU 148/9-1 to TT. We would like to express our gratitude to both Christophe Lécuyer and to a second anonymous reviewer for their constructive and thoughtful comments that helped to improve the manuscript.

Appendix A. Supplementary material

Data are available as Supplementary Material in the appendix. The appendix consists of four tables (Table S1-S4) and one figure (Fig. S1). Table S1 contains the data underlying the $^{18}O/^{16}O$ profiles in Fig. 3. The values were derived by integrating the counts of an area (marked as white boxes in Fig. 2) of 4 μm in the x-direction and 30–38 μm in the y-direction, depending on the thickness of the resin-covered area, which was excluded from the plot. Table S2 and S3 provide the Raman spectral parameters (FWHM and Raman shift) of the references and samples, respectively, plotted in Fig. 4. The raw data underlying the calculation of the spectral resolution, which was used to correct the bandwidth of all data for finite width effects (Tanabe and Hiraishi, 1980), are given in Table S4. Fig. S1 shows the fluorine distribution mosaic image consisting of 9 individual isotope distribution maps, each 40 x 40 μm^2. The mosaic image was obtained from of a CB sample that reacted at 90 °C for 30 d in an FWS solution using nanoSIMS.

Supplementary material to this article can be found online at https://doi.org/10.1016/j.gca.2024.04.004.

References

Amiot, R., Lécuyer, C., Buffetaut, E., Escarguel, G., Fluteau, F., Martineau, F., 2006. Oxygen isotopes from biogenic apatites suggest widespread endothermy in cretaceous dinosaurs. Earth Planet. Sci. Lett. 246, 41–54.
Asjadi, F., Geisler, T., Salahi, I., Euler, H., Mobasherpour, I., 2019. Ti-substituted hydroxylapatite precipitated in the presence of titanium sulfate: a novel photocatalyst? Am. J. Chem. Appl. 6, 1–10.
Aufort, J., Gervais, C., Ségalen, L., Labourdette, N., Coelho-Diogo, C., Baptiste, B., Beyssac, O., Amiot, R., Lécuyer, C., Balan, E., 2019. Atomic scale transformation of bone in controlled aqueous alteration experiments. Palaeogeogr. Palaeoclimatol. Palaeoecol. 526, 80–95.
Baertschi, P., 1976. Absolute ^{18}O content of standard mean ocean water. Earth Planet. Sci. Lett. 31, 341–344.
Barrick, R.E., Showers, W.J., 1994. Thermophysiology of *Tyrannosaurus rex*: evidence from oxygen isotopes. Science 265, 222–224.
Barthel, J.H., Fougerouse, D., Geisler, T., Rust, J., 2020. Fluoridation of a lizard bone embedded in Dominican amber suggests open-system behavior. PLoS ONE 15, e0228843.
Berna, F., Matthews, A., Weiner, S., 2004. Solubilities of bone mineral from archaeological sites: the recrystallization window. J. Archaeol. Sci. 31, 867–882.
Bernard, A., Lécuyer, C., Vincent, P., Amiot, R., Bardet, N., Buffetaut, E., Cuny, G., Fourel, F., Martineau, F., Mazin, J.-M., Prieur, A., 2010. Regulation of body temperature by some Mesozoic marine reptiles. Science 328, 1379.
Blake, R.E., O'Neil, J.R., Garcia, G.A., 1997. Oxygen isotope systematics of biologically mediated reactions of phosphate: I. Microbial degradation of organophosphorus compounds. Geochim. Cosmochim. Acta 61, 4411–4422.
Chang, S.J., Blake, R.E., Colman, A.S., 2021. Oxygen isotope exchange rates between phosphate and water catalyzed by inorganic pyrophosphatase: implications for the biogeochemical cycle of phosphorus. Earth Planet. Sci. Lett. 570, 117071.

Collins, M.J., Nielsen-Marsh, C.M., Hiller, J., Smith, C.I., Roberts, J.P., Prigodich, R.V., Wess, T.J., Csapò, M., A.R., Turner-Walker, G., 2002. The survival of organic matter in bone: a review. Archaeometry 44, 383–394.
Cook, P.J., 1973. The phosphate content of sediments at sites 259-263 Deep Sea Drilling Project, Eastern Indian Ocean. Geoscience Australia, Canberra. Bureau of Mineral Resources, Geology and Geophysics. Record 1973/135.
Dal Sasso, G., Asscher, Y., Angelini, I., Nodari, L., Artioli, G., 2018. A universal curve of apatite crystallinity for the assessment of bone integrity and preservation. Sci. Rep. 8, 12025.
Dauphin, Y., 2022. Vertebrate taphonomy and diagenesis: implications of structural and compositional alterations of phosphate biominerals. Minerals 12, 180.
De Graaf, S., Vonhof, H.B., Weissbach, T., Wassenburg, J.A., Levy, E.J., Kluge, T., Haug, G.H., 2020. A comparison of isotope ratio mass spectrometry and cavity ring-down spectroscopy techniques for isotope analysis of fluid inclusion water. Rapid Comm. Mass Spec. 34, e8837.
De Graaf, S., Vonhof, H.B., Levy, E.J., Markowska, M., Haug, G.H., 2021. Isotope ratio infrared spectroscopy (IRIS) analysis of water samples without memory effects. Rapid Comm. Mass Spec. 35, e9055.
Elorza, J., Astibia, H., Murelaga, X., Pereda-Suberbiola, X., 1999. Francolite as a diagenetic mineral in dinosaur and other upper Cretaceous reptile bones (Lano, Iberian Peninsula): microstructural, petrological and geochemical features. Cretac. Res. 20, 169–187.
Feng, D., Tütken, T., Löffler, N., Tröster, G., Pack, A., 2022. Isotopically anomalous metabolic oxygen in marine vertebrates as physiology and atmospheric proxy. Geochim. Cosmochim. Acta 328, 85–102.
Fernández-Seara, M.A., Wehrli, S.L., Wehrli, F.W., 2002. Diffusion of exchangeable water in cortical bone studied by nuclear magnetic resonance. Biophys. J. 82, 522–529.
Filippelli, G.M., 2002. The global phosphorus cycle. In: Kohn, M.J., Rakovan, J., Hughes, J. (Eds.), Phosphates: Geochemical, Geobiological and Materials Importance. De Gruyter Berlin, Boston, pp. 391–426. https://doi.org/10.1515/9781501509636-013.
Gehler, A., Tütken, T., Pack, A., 2011. Triple oxygen isotope analysis of bioapatite as tracer for diagenetic alteration of bones and teeth. Palaeogeogr. Palaeoclimatol. Palaeoecol. 310, 84–91.
Gehler, A., Tütken, T., Pack, A., 2012. Oxygen and carbon isotope variations in a modern rodent community – implications for palaeoenvironmental reconstructions. PLoS ONE 7, e49531.
Geisler, T., Kasioptas, A., Menneken, M., Perdikouri, C., Putnis, A., 2009. A preliminary *in situ* Raman spectroscopic study of the oxygen isotope exchange kinetics between H_2O and $(PO_4)_{aq}$. J. Geochem. Explor. 101, 37.
Geisler, T., Menneken, T., 2021. Raman spectroscopy in fossilization research: basic principles, applications in paleontology, and a case study on an acanthodian fish spine. In: Sander, P.M., McCoy, V.E., Gee, C.T. (Eds.), Fossilization: Understanding the Material Nature of Ancient Plants and Animals. John Hopkins University Press, Baltimore, pp. 73–114.
Goodwin, M.B., Grant, P.G., Bench, G., Holroyd, P.A., 2007. Elemental composition and diagenetic alteration of dinosaur bone: distinguishing micron-scale spatial and compositional heterogeneity using PIXE. Palaeogeogr. Palaeoclimatol. Palaeoecol. 253, 458–476.
Hedges, R.E.M., 2002. Bone diagenesis: an overview of processes. Archaeometry 44, 319–328.
Herwartz, D., Tütken, T., Münker, C., Jochum, K.P., Stoll, B., Sander, P.M., 2011. Timescales and mechanisms of REE and Hf uptake in fossil bones. Geochim. Cosmochim. Acta 75, 82–105.
Hinz, E.A., Kohn, M.J., 2010. The effect of tissue structure and soil chemistry on trace element uptake in fossils. Geochim. Cosmochim. Acta 74, 3213–3231.
Hubert, J.F., Panish, P.T., Chure, D.J., Prostak, K.S., 1996. Chemistry, microstructure, petrology, and diagenetic model of Jurassic dinosaur bones, Dinosaur National Monument. Utah. J. Sediment. Res. 66, 531–547.
Iacumin, P., Bocherens, H., Mariotti, A., Longinelli, A., 1996. Oxygen isotope analyses of co-existing carbonate and phosphate in biogenic apatite: a way to monitor diagenetic alteration of bone phosphate? Earth Planet. Sci. Lett. 142, 1–6.
Iacumin, P., Rossi, M., Selmo, E., Venturelli, G., 2022. Oxygen isotopes in carbonate and phosphate of modern mammal bioapatite: new data and critical revision after about 25 years from the first recognitions. Minerals 12, 1204.
Jans, M.M., 2008. Microbial bioerosion of bone - a review. In: Wisshak, M., Tapanila, L. (Eds.), Current Developments in Bioerosion. Erlangen Earth Conference Series. Springer, Berlin, Heidelberg, pp. 397–413.
Keenan, S.W., 2016. From bone to fossil: a review of the diagenesis of bioapatite. Am. Min. 101, 1943–1951.
Keenan, S.W., Engel, A.S., 2017. Early diagenesis and recrystallization of bone. Geochim. Cosmochim. Acta 196, 209–223.
Kelly, P.J., Bassingthwaighte, J.B., 1977. Studies on bone ion exchanges using multiple-tracer indicator-dilution techniques. Fed. Proc. 36, 2634–2639.
Kohn, M.J., 1996. Predicting animal δ^{18} O: accounting for diet and physiological adaptation. Geochim. Cosmochim. Acta 60, 4811–4829.
Kohn, M.J., 2008. Models of diffusion-limited uptake of trace elements in fossils and rates of fossilization. Geochim. Cosmochim. Acta 72, 3758–3770.
Kohn, M.J., Moses, R.J.M., 2013. Trace element diffusivities in bone rule out simple diffusive uptake during fossilization but explain *in vivo* uptake and release. Proc. Nat. Acad. Sci. 110, 419–424.
Kolodny, Y., Luz, B., Sander, M., Celemens, W.A., 1996. Dinosaur bones: fossils or pseudomorphs? The pitfalls of physiology reconstruction from apatitic fossils. Palaeogeogr. Palaeoclimatol. Palaeoecol. 126, 161–171.
Konrad-Schmolke, M., Halama, R., Wirth, R., Thomen, A., Klitscher, N., Morales, L., Schreiber, A., Wilke, F.D.H., 2018. Mineral dissolution and reprecipitation are mediated by an amorphous phase. Nat. Commun. 9, 1637.
Kral, A.G., Ziegler, A., Tütken, T., Geisler, T., 2021. Experimental aqueous alteration of cortical bone microarchitecture analyzed by quantitative micro-computed tomography. Front. Earth Sci. 9, 609496.
Kral, A.G., Lagos, M., Guagliardo, P., Tütken, T., Geisler, T., 2022. Rapid alteration of cortical bone in fresh- and seawater solutions visualized and quantified from the millimeter down to the atomic scale. Chem. Geol. 602, 121060.
Lanfranco, A.M., Schofield, P.F., Murphy, P.J., Hodson, M.E., Mosselmans, J.F.W., Valsami-Jones, E., 2003. Characterization and identification of mixed-metal phosphates in soils: the application of Raman spectroscopy. Mineral. Mag. 67, 1299–1316.
Lécuyer, C., Grandjean, P., Sheppard, S.M.F., 1999. Oxygen isotope exchange between dissolved phosphate and water at temperatures ≤135°C: inorganic versus biological fractionations. Geochim. Cosmochim. Acta 63, 855–862.
Lécuyer, C., Amiot, R., Touzeau, A., Trotter, J., 2013. Calibration of the phosphate δ^{18}O thermometer with carbonate–water oxygen isotope fractionation equations. Chem. Geol. 347, 217–226.
Lécuyer, C., Flandrois, J.-P., 2023. Mitigation of the diagenesis risk in biological apatite δ^{18}O interpretation. Palaeogeogr. Palaeoclimatol. Palaeoecol. 630, 111812.
Liang, Y., Blake, R.E., 2007. Oxygen isotope fractionation between apatite and aqueous-phase phosphate: 20–45 °C. Chem. Geol. 238, 121–133.
Lin, A.-M.-R., Antonaiadis, D.A., Dutton, R.W., 1981. The oxidation rate dependence of oxidation-enhanced diffusion of boron and phosphorus in silicon. J. Electrochem. Soc. 128, 1131.
Longinelli, A., 1984. Oxygen isotopes in mammal bone phosphate: a new tool for paleohydrological and paleoclimatological research? Geochim. Cosmochim. Acta 48, 385–390.
Mosiman, D.S., Sutrisno, A., Fu, R., Mainas, J.B., 2021. Internalization of fluoride in hydroxyapatite nanoparticles. Environ. Sci. Technol. 55, 2639–2651.
Müller, T.E., Watson, B.E., Harrison, M.T., 2010. Applications of diffusion data to high-temperature earth systems. Rev. Mineral. Geochem. 72, 997–1038.
Nemliher, J., Kurvits, T., Kallaste, T., Puura, I., 2004. Apatite varieties in the shell of the Cambrian lingulate brachiopod *Obolus apollinis* Eichwald. Proc. Est. Acad. Sci. Geology 53, 246–256.
Nielsen-Marsh, C.M., Hedges, R.E.M., 2000. Patterns of diagenesis in bone I: the effects of site environments. J. Archaeol. Sci. 27, 1139–1150.
O'Neil, J.R.O., Vennemann, T.W., McKenzie, W.F., 2003. Effects of speciation on equilibrium fractionations and rates of oxygen isotope exchange between $(PO_4)_{aq}$ and H_2O. Geochim. Cosmochim. Acta 67, 3135–3144.
Oxmann, J.F., Schwendenmann, L., 2014. Quantification of octacalcium phosphate, authigenic apatite and detrital apatite in coastal sediments using differential dissolution and standard addition. Ocean Sci. 10, 571–585.
Pack, A., Gehler, A., Sussenberger, A., 2013. Exploring the usability of isotopically anomalous oxygen in bones and teeth as paleo-CO_2-barometer. Geochim. Cosmochim. Acta 102, 306–317.
Pasteris, J.D., Ding, D.Y., 2009. Experimental fluoridation of nanocrystalline apatite. Am. Min. 94, 53–63.
Peccati, F., Bernocco, C., Ugliengo, P., Corno, M., 2018. Properties and reactivity toward water of a type carbonated apatite and hydroxyapatite surfaces. J. Phys. Chem. C 122, 3934–3944.
Pellegrini, M., Lee-Thorp, J.A., Donahue, R.E., 2011. Exploring the variation of the $\delta^{18}O_p$ and $\delta^{18}O_c$ relationship in enamel increments. Palaeogeogr. Palaeoclimatol. Palaeoecol. 310, 71–83.
Penel, G., Leroy, G., Rey, C., Sombret, B., Huvenne, J.P., Bres, E., 1997. Infrared and Raman microspectrometry study of fluor-fluor-hydroxy and hydroxy-apatite powders. J. Mater. Sci.: Mater. Med. 8, 271–276.
Pfretzschner, H.-U., 2001a. Pyrite in fossil bone. Neues Jahrb. für Geol. Paläontol. - Abh. 220, 1–23.
Pfretzschner, H.-U., 2001b. Iron oxides in fossil bone. Neues Jahrb. für Geol. Paläontol. - Abh. 220, 417–429.
Pfretzschner, H.-U., 2004. Fossilization of Haversian bone in aquatic environments. C R Palevol. 3, 605–616.
Pfretzschner, H.-U., 2006. Collagen gelatinization: the key to understand early bone-diagenesis. Palaeontogr. Abt. A 278, 135–148.
Pfretzschner, H.-U., Tütken, T., 2011. Rolling bones - taphonomy of Jurassic dinosaur bones inferred from diagenetic microcracks and mineral infillings. Palaeogeogr. Palaeoclimatol. Palaeoecol. 310, 117–123.
Piga, G., Goncalves, D., Thompson, T.J.U., Brunetti, A., Malgosa, A., Enzo, S., 2016. Understanding the crystallinity indices behavior of burned bones and teeth by ATR-IR and XRD in the presence of bioapatite mixed with other phosphate and carbonate phases. Int. J. Spectrosc. 2016, 4810149.
Prieto, M., 2009. Thermodynamics of solid solution-aqueous solution systems. Rev. Mineral. Geochem. 70, 47–85.
Procopio, N., Mein, C.A., Starace, S., Bonicelli, A., Williams, A., 2021. Bone diagenesis in short timescales: insights from an exploratory proteomic analysis. Biology 10, 460.
Putnis, A., 2002. Mineral replacement reactions: from macroscopic observations to microscopic mechanisms. Mineral. Mag. 66, 689–708.
Putnis, A., 2009. Mineral replacement reactions. Rev. Mineral. Geochem. 70, 87–124.
Putnis, A., 2021. Fluid-mineral interactions: controlling coupled mechanisms of reaction, mass transfer and deformation. J. Petrol. 62, egab092.
Putnis, A., Putnis, C.V., 2007. The mechanism of reequilibration of solids in the presence of a fluid phase. J. Solid State Chem. 180, 1783–1786.

Putnis, C.V., Putnis, A., 2022. A mechanism of ion exchange by interface-coupled dissolution-precipitation in the presence of an aqueous fluid. J. Cryst. Growth 600, 126840.
Qiao, W., Liu, Q., Li, Z., Zhang, H., Chen, Z., 2017. Changes in physicochemical and biological properties of porcine bone derived hydroxyapatite induced by the incorporation of fluoride. Sci. Technol. Adv. Mater. 18, 110–121.
Ren, X., Li, J., Cao, X., Wang, B., Zhang, Y., 2019. Synergistic effect of internal electric field and oxygen vacancy on the photocatalytic activity of BiOBrxI1−x with isomorphous fluorine substitution. J. Colloid Interface Sci. 554, 500–511.
Renard, F., Royne, A., Putnis, C.V., 2019. Timescales of interface-coupled dissolution-precipitation reactions on carbonates. Geosci. Front. 10, 17–27.
Rogers, K.D., Zioupos, P., 1999. The bone tissue of the rostrum of a *Mesoplodon densirostris* whale: a mammalian biomineral demonstrating extreme texture. J. Mater. Sci. Lett. 18, 651–654.
Ruiz-Agudo, E., Putnis, C.V., Putnis, A., 2014. Coupled dissolution and precipitation at mineral–fluid interfaces. Chem. Geol. 383, 132–146.
Schindelin, J., Arganda-Carreras, I., Frise, E., Kaynig, V., Longair, M., Pietzsch, T., Preibisch, S., Rueden, C., Saalfeld, S., Schmid, B., Tinevez, J.-Y., White, D.J., Hartenstein, V., Eliceiri, K., Tomancak, P., Cardone, A., 2012. Fiji: an open-source platform for biological-image analysis. Nat. Methods 9, 676–682.
Seon, N., Amiot, R., Suan, G., Lécuyer, C., Fourel, F., Demaret, F., Vincon-Laugier, A., Charbonnier, S., Vincent, P., 2022. Intra-skeletal variability in phosphate oxygen isotope composition reveals regional heterothermies in marine vertebrates. Biogeosciences 19, 2671–2681.
Simpson, R., Cooper, D.M.L., Swanston, T., Coulthard, I., Varney, T.L., 2021. Historical overview and new directions in bioarchaeological trace element analysis: a review. Archaeol. Anthropol. Sci. 13, 24.
Spry, A., 1969. Metamorphic textures, first ed. Pergamon Press, Oxford.
Sternitzke, V., Kaegi, R., Audinot, J.-N., Lewin, E., Hering, J.G., Johnson, A.C., 2012. Uptake of fluoride from aqueous solution on nano-sized hydroxyapatite: examination of a fluoridated surface layer. Environ. Sci. Technol. 46, 802–809.
Stoskopf, M.K., Barrick, R.E., Showers, W.J., 2001. Oxygen isotope variability in bones of wild caught and constant temperature reared sub-adult American alligators. J. Therm. Biol. 26, 183–191.
Tanabe, K., Hiraishi, J., 1980. Correction of finite slit width effects on Raman line widths. Spectrochim. Acta A Mol. Biomol. Spectrosc. 36, 341–344.
Thomas, D.B., Fordyce, R.E., Frew, R.D., Gordon, K.C., 2007. A rapid, non-destructive method of detecting diagenetic alteration in fossil bone using Raman spectroscopy. J. Raman Spectrosc. 38, 1533–1537.
Thomas, D.B., McGoverin, C.M., Fordyce, R.E., Frew, R.D., Gordon, K.C., 2011. Raman spectroscopy of fossil bioapatite — a proxy for diagenetic alteration of the oxygen isotope composition. Palaeogeogr. Palaeoclimatol. Palaeoecol. 310, 62–70.
Trueman, C.N., Martill, D.M., 2002. The long–term survival of bone: the role of bioerosion. Archaeometry 44, 371–381.
Trueman, C.N., Privat, K., Field, J., 2008. Why do crystallinity values fail to predict the extent of diagenetic alteration of bone mineral? Palaeogeogr. Palaeoclimatol. Palaeoecol. 266, 160–167.
Trueman, C.N., Tuross, N., 2002. Trace elements in recent and fossil bone apatite. Rev. Mineral. Geochem. 48, 489–521.
Trueman, C.N., Behrensmeyer, A.K., Tuross, N., Weiner, S., 2004. Mineralogical and compositional changes in bones exposed on soil surfaces in Amboseli National Park, Kenya: diagenetic mechanisms and the role of sediment pore fluids. J. Archaeol. Sci. 31, 721–739.
Turner-Walker, G., 2011. The mechanical properties of artificially aged bone: probing the nature of the collagen–mineral bond. Palaeogeogr. Palaeoclimatol. Palaeoecol. 310, 17–22.
Turner-Walker, G., 2019. Light at the end of the tunnels? The origins of microbial bioerosion in mineralised collagen. Palaeogeogr. Palaeoclimatol. Palaeoecol. 529, 24–38.
Tütken, T., Vennemann, T.W., Pfretzschner, H.-U., 2008. Early diagenesis of bone and tooth apatite in fluvial and marine settings: constraints from combined oxygen isotope, nitrogen and REE analysis. Palaeogeogr. Palaeoclimatol. Palaeoecol. 266, 254–268.
Tzaphlidou, M., 2008. Bone architecture: collagen structure and calcium/phosphorus maps. J Biol. Phys. 34, 39–49.
Vaissier Welborn, V., 2021. Environment-controlled water adsorption at hydroxyapatite/collagen interfaces. Phys. Chem. Chem. Phys. 23, 13789–13796.
Weber, K., Weber, M., Menneken, M., Kral, A.G., Mertz-Kraus, R., Geisler, T., Vogl, J., Tütken, T., 2021. Diagenetic stability of non-traditional stable isotope systems (Ca, Sr, Mg, Zn) in teeth – an *in-vitro* alteration experiment of biogenic apatite in isotopically enriched tracer solution. Chem. Geol. 572, 120196.
White, L., Booth, T.J., 2014. The origin of bacteria responsible for bioerosion to the internal bone microstructure: results from experimentally-deposited pig carcasses. Forensic Sci. Int. 239, 92–102.
Wierzbowski, H., 2021. Advances and challenges in palaeoenvironmental studies based on oxygen isotope composition of skeletal carbonates and phosphates. Geosciences 11, 419.
Wopenka, B., Pasteris, J.D., 2005. A mineralogical perspective on the apatite in bone. Mater. Sci. Eng. C. - Bio. S. 25, 131–143.
Wudarska, A., Wiedenbeck, M., Slaby, E., Lempart-Drozd, M., Harris, C., Joachimski, M. M., Lécuyer, C., MacLeod, K.G., Pack, A., Vennemann, T., Couffignal, F., Feng, D., Glodny, J., Kusebauch, C., Mayanna, S., Rocholl, A., Speir, L., Sun, Y., Wilke, F.D.H., 2022. Inter-laboratory characterisation of apatite reference materials for oxygen isotope analysis and associated methodological considerations. Geostand. Geoanal. Res. 46, 277–306.
Xia, F., Brugger, J., Chen, G., Ngothai, Y., O'Neill, B., Putnis, A., Pring, A., 2009. Mechanism and kinetics of pseudomorphic mineral replacement reactions: a case study of the replacement of pentlandite by violarite. Geochim. Cosmochim. Acta 73, 1945–1969.
Zazzo, A., Lécuyer, C., Mariotti, A., 2004. Experimentally-controlled carbon and oxygen isotope exchange between bioapatites and water under inorganic and microbially-mediated conditions. Geochim. Cosmochim. Acta 68, 1–12.
Zhu, Y., Zhang, X., Chen, Y.D., Xie, Q., Lan, J., et al., 2009. A comparative study on the dissolution and solubility of hydroxylapatite and fluorapatite at 25 °C and 45 °C. Chem. Geol. 268, 89–96.